

Main Manuscript for

Ionization and electron excitation of fullerene molecules in a carbon nanotube. A variable temperature/voltage transmission electron microscopic study

Dongxin Liu,[†] Satori Kowashi,[†] Takayuki Nakamuro,^{*,†} Dominik Lungerich,^{†,‡,||} Kaoru Yamanouchi,[†] Koji Harano,^{*,†} Eiichi Nakamura^{*,†}

[†]Department of Chemistry, The University of Tokyo, 7-3-1 Hongo, Bunkyo-ku, Tokyo 113-0033, Japan

[‡]Center for Nanomedicine (CNM), Institute for Basic Science (IBS), IBS Hall, 50 Yonsei-ro, Seodaemun-gu, Seoul, 03722, South Korea.

^{||}Graduate Program of Nano Biomedical Engineering (NanoBME), Advanced Science Institute, Yonsei University, Seoul, 03722, South Korea.

*Correspondence to: Takayuki Nakamuro, Koji Harano, Eiichi Nakamura

Email: muro@chem.s.u-tokyo.ac.jp, harano@chem.s.u-tokyo.ac.jp, nakamura@chem.s.u-tokyo.ac.jp

Author Contributions: E.N., K.H. and T.N. supervised the project. D.Liu and S.K. carried out the TEM experiments and analyzed the data with T.N., D. Lungerich, K.Y., K.H. and E.N. D. Liu, T.N., K.H. and E.N. cowrote the paper. All authors discussed the results and commented on the manuscript.

Competing Interest Statement: Authors declare no competing interests.

Classification: PHYSICAL SCIENCE, Chemistry

Keywords: excited state chemistry, radiation chemistry, radical cation, fullerene, transmission electron microscopy

This PDF file includes:

Main Text
Figures 1 to 9
Tables 1

Abstract

There is increasing attention to chemical applications of transmission electron microscopy, which is often plagued by radiation damage. The damage in organic matter predominantly occurs via ionization (radiolysis). Although radiolysis is highly important, previous studies on radiolysis have largely been descriptive and qualitative, lacking in such fundamental information as the product structure, the influence of the energy of the electrons, and the reaction kinetics. We need a chemically well-defined system to obtain such data, and have chosen as a model a variable-temperature and variable-voltage (VT/VV) study of the dimerization of a van der Waals dimer [60]fullerene (C₆₀) to C₁₂₀ in a carbon nanotube (CNT) as studied for individual reaction events at atomic resolution. We report here the identification of five reaction pathways that serve as mechanistic models of radiolysis damage. Two of them occur via a radical cation of the specimen generated by specimen ionization, and three involve singlet or triplet excited states of the specimen, as initiated by electron excitation of the CNT followed by energy transfer to the specimen. The pathways were distinguished by the pre-exponential factor and the Arrhenius activation energy. The prototypal reaction path is the radical cation reaction that we saw at <200 K, but, at >350 K, the excited-state reactions dominate. The results illustrate the importance of VT/VV kinetic analysis in the studies of radiation damage, and show that chemical ionization and

electron excitation are inseparable but different mechanisms of radiation damage, which has so far been classified loosely under the single term “ionization.”

Significance Statement

The destruction of specimen molecules by an electron beam (e-beam) is either beneficial as in mass spectrometry capitalizing on ion formation, or deleterious as in electron microscopy. In the latter application, the e-beam not only produces the specimen image but also causes information loss upon prolonged irradiation. However, the atomistic mechanism of such loss has been unclear. Performing single-molecule kinetic analysis of C₆₀ dimerization in a carbon nanotube (CNT) under variable-temperature, variable-voltage conditions, we found three reactive species reacting competitively as the voltage and the properties of the CNT were changed. Thus, we identified radical cation, singlet, and triplet excited states, characterized by five different sets of the activation energy and pre-exponential factor. The key enabler of the research was in situ cinematic recording of the whole reaction process, suggesting an upcoming new era of “cinematic chemistry.”

Main Text

Introduction

Since the time of the Knoll/Ruska invention of transmission electron microscopy (TEM) (1), electron microscopy has suffered from information loss during observation often ascribed to the structural changes of a specimen into a different substance, known as radiation damage (2). As summarized recently by Egerton (3), the electron-beam (e-beam) damage in organic matter predominantly occurs via processes triggered by ionization (radiolysis). Although radiolysis is highly important, studies on radiolysis have largely been descriptive and qualitative because of the complexity of the process and the difficulty in quantifying the changes under variable-temperature and variable-voltage (VT/VV) conditions. The first step of the process involves electron-impact ionization (EII), which removes an electron to form a radical cation (RC) of the specimen, or possibly also electron-impact excitation (EIE) where the electron does not fly away to the vacuum but stays in a higher antibonding state in the system. The processes were recently studied in depth for the first time by a thorough quantum chemical study (4). There has been, however, a paucity of experimental mechanistic information; that is, how a specimen is transformed to what product with what level of activation energy and frequency at what acceleration voltage. Single molecules encapsulated in a carbon nanotube (CNT) have often been observed either stably or undergoing well-defined chemical transformations (5,6,7,8,9), and it is primarily because the damage due to secondary electrons is a minimum (10). Drawing an analogous specimen stabilization by a thin metallic coating or deposition on a conductive indium tin oxide substrate in scanning electron microscopy (SEM) (11), we can consider that the electron-rich CNT (Fig. 1A) interacts with the specimen molecules and protects them from ionization by filling in the electron vacancy in the RC. In light of the recent characterization of singlet and triplet excitons of CNTs (Fig. 1A) (12), we conjectured also that the CNT exciton would excite a molecule in the CNT via energy transfer (ENT) (Fig. 2A) (13,14). Electron excitation of graphene under TEM conditions has also been suggested recently (15,16).

We report here the VT/VV kinetic study of the dimerization of a van der Waals (vdW) dimer [60]fullerene (C₆₀) to C₁₂₀ in a CNT (17,18,19), in which we found five competing reaction pathways that serve as model pathways of radiolysis damage (Fig. 1B–F). We found a marked influence of the temperature, the acceleration voltage, and the properties of the CNT—pristine

(prCNT), oxidized (oxCNT), or damaged CNT (dmCNT) (Fig. 2B). They have been distinguished by the pre-exponential factor (PEF) and the Arrhenius activation energy (E_a). The most frequently occurring reaction was found to occur via singlet (S_1) or triplet (T_1) species generated by ENT from a CNT exciton (Fig. 1B,C) (3). The triplet reaction also occurs when we use an oxidized CNT, which is known to form a triplet exciton (Fig. 1D). Electrons of 60 keV in energy cannot energize prCNT to the triplet state, and instead directly ionize C_{60} into RC, which is then reduced by the CNT to a mixture of S_1 and T_1 states (Fig. 1E). This process illustrates how prCNT protects the specimen from radiolysis by “grounding” (Fig. 2C) and accounts for the stability of a variety of molecules having low-lying highest occupied molecular orbitals, such as saturated hydrocarbons (20), amides (21), alcohols (22), and inorganic salts encapsulated in a CNT (23,24). We observed the RC when the reaction was performed in a heavily damaged CNT (Fig. 1F). The VT/VV behavior of the kinetics agrees with the competitive occurrence of electron excitation and ionization, but not with the atomic displacement damage mechanism, which is the major cause of radiation damage in conductive inorganic materials (25).

Results

Light transfers its energy to a zero-dimensional (0D) material via an electric dipole transition (EDT) mechanism with conservation of spin angular momentum (Fig. 1A) (26), and the excited species undergo intersystem crossing (ISC) (27) and ENT (28). Being a particle wave, e-beam lacks EDT capability, and causes predominantly plasmon excitation, EII, and atom displacement via momentum transfer (29). EIE of CNT occurs with conservation of spin angular momentum (30). CNT resembles 0D materials due to van Hove singularities (Fig. 1A) (31), and we envisaged that the CNT exciton transfers energy to C_{60} encapsulated in CNT (Fig. 2A). We monitored the reaction using single-molecule atomic-resolution time-resolved electron microscopic technique (SMART-EM) under VT/VV conditions at 103–493 K and 60–120 keV (10,19).

The thermally forbidden [2 + 2] dimerization of vdW (C_{60})₂ does not take place at temperatures <800 K (32). The reaction commences upon photo-irradiation of C_{60} film or solid (33,34), also occurs upon electron irradiation (Fig. 2A, box). Further irradiation converts the initially formed [2 + 2] dimer eventually to a short CNT (18) via retro [2 + 2] cycloaddition and a series of Stone–Wales rearrangements (Fig. 3A) (35).

In 2011, C_{60} dimerization in CNTs was reported to take place even with 20-keV irradiation, although it then requires a 100-times larger electron dose than at 80 kV (36). The 20-keV energy is far lower than the threshold voltage of carbon atom displacement (CAD, knock-on displacement), and the data suggests a mechanism not going through CAD. A 60-keV electron beam was recently reported to cause reactions of C_{60} sandwiched between two graphene sheets – loss of one carbon atom to form a C_{118} (quasi) dimer via C_{59} (37). This may suggest a difference between a 1D CNT and gapless 2D graphene that lacks van Hove singularities (Fig. 1A). This is briefly examined in the present study.

VT-SMART-EM imaging is an emerging experimental tool for the study of kinetics and thermodynamics of individual chemical events (19, 22, 38), and it has provided direct experimental proof of the Rice–Ramsperger–Kassel–Marcus theory (39). In this study, we performed VT-SMART-EM imaging under VV conditions (VT/VV-SMART-EM). Following the reaction conditions developed previously (19), we encapsulated the fullerene molecule in a bundle of pr-, ox-, or dmCNTs, 1.3–1.4 nm in diameter (40), by heating them together at 823 K for 15 h in vacuo. A specimen was deposited on a TEM grid and the time evolution of the [2 + 2] cycloaddition of a (C_{60})₂@CNT was visually monitored with a frame rate of two frames per second (s) under e-beam irradiation at 120, 100, 80, and 60 kV, with a constant electron dose rate (EDR) of $3.1 \times 10^5 \text{ e}^- \text{ nm}^{-2} \text{ s}^{-1}$ for 120 kV and $5.0 \times 10^6 \text{ e}^- \text{ nm}^{-2} \text{ s}^{-1}$ for 60–100 kV throughout this study.

Note that the reaction rate per electron measured in the present work is not affected by the variation of EDR as previously reported (19).

The cycloaddition event was characterized by the change in intermolecular distance from 1.00 nm for the vdW dimer to 0.90 nm for the cycloadduct (Fig. 3B), and the E_a and PEF were determined (19). The [2 + 2] cycloadduct features a strained cyclobutane ring in the middle and reverts to two molecules of C_{60} upon heating at >500 K, thus providing compelling chemical evidence that the adduct is the C_{120} cycloadduct (Fig. 3A).

Singlet Dimerization of a $(C_{60})_2@CNT$. Unlike light that can transfer its entire energy for electron excitation of molecules via an EDT mechanism, the momentum transfer mechanism of an e-beam can transfer its energy to molecules very inefficiently. To assess how inefficient it would be, and to know the consequence of poor efficiency, we performed the kinetic analysis at an acceleration voltage decreasing stepwise from 120 keV to 60 keV.

We first found that a beam of 100–120-keV electrons excites a $(C_{60})_2$ vdW dimer to the S_1 state – a pathway expected because the EIE with high-energy e-beam occurs with conservation of spin angular momentum (30). Rather unexpectedly, however, the S_1 path was unavailable with a beam of 80-keV electron, which instead opened a T_1 path, suggesting that the 80-keV electron generated a triplet CNT exciton. ISC from a singlet exciton of CNT to triplet was documented recently (12). Given the reported S_0/S_1 energy difference of ~2.5 eV for C_{60} (41), we estimated that the 100–120-keV e-beam transferred at most ~2.5 eV to C_{60} , that is, 2 to 2.5×10^{-5} of its kinetic energy (2.5 eV/100–120 keV). Similarly, the S_0/T_1 energy difference of ~1.5 eV for C_{60} (41) suggests that at most $\sim 1.9 \times 10^{-5}$ of the 80 keV was utilized for C_{60} excitation.

Taking these numbers at 80–120 keV into account, we expect that a beam of 60-keV electrons cannot excite the CNT, which typically has a bandgap of 1 eV, and hence we expect no dimerization at 60 keV. Interestingly, excited-state dimerization at 60 keV did take place, albeit very infrequently, suggesting that the excited states are not generated via ENT from the CNT but via the RC (Fig. 1E).

In Fig. 4, we summarize all the data of the dimerization at 60–120 keV at 443–493 K. The raw data at 443 K are shown in Fig. 4A, where we plot the number of dimerization events observed at intervals of $8.0 \times 10^6 e^- nm^{-2}$ irradiation against the total electron dose (TED) up to $3.0 \times 10^8 e^- nm^{-2}$ (for 60 s). After in situ monitoring of the reactions of 39–55 C_{60} dimerization events at acceleration voltages of 120 (black), 100 (red), 80 (blue), and 60 kV (green, Fig. 4A), we observed three features. First, each reaction event takes place stochastically (42). Second, the occurrence of the events follows the first-order kinetics shown in Fig. 4B and C, where the $1 - P$ and $\ln(1 - P)$ values are plotted against TED (P = normalized conversion of C_{60}). Third, we find three different kinetic profiles.

The rate constants (k) at 100 kV are summarized in Fig. 4D. The error is arguably large, for several reasons. The CNT is a mixture of entities having different chirality indexes (i.e., the diameters) (43) and, under different physicochemical environments, molecular packing in CNTs changes as the reaction proceeds.

Using the rate constants k obtained at five temperatures, we plotted the Arrhenius plot to obtain the activation energy (E_a , slope) and PEF (y-intercept) (Fig. 4E). The E_a values at 120 and 100 kV are nearly identical, 33.5 ± 6.8 and 32.9 ± 6.0 kJ mol $^{-1}$, respectively, hence suggesting the same reaction mechanism. The reaction in CNTs under 120 kV (PEF = $3.9 \times 10^{-4} (e^-)^{-1} nm^2$) occurs more frequently than the reaction under 100 kV (PEF = $5.9 \times 10^{-5} (e^-)^{-1} nm^2$).

The reaction at 80 kV took place with E_a and PEF values essentially the same as those of the T_1 reaction mediated by a triplet-sensitizing oxCNT (see below). We therefore consider the

reaction to take place via T_1 . The T_1 species forms less frequently (y-intercept = PEF) but is more reactive than the S_1 species (slope = E_a). An orbital diagram of the concerted singlet cycloaddition is illustrated in Fig. 4F.

The reaction at 60 kV was markedly slower at ~400 K than the reaction at 100–120 kV (Fig. 4B and Fig. S3). The Arrhenius plot (green, Fig. 4E) deviates from linearity, and we surmise that the kinetics reflects competing S_1 and T_1 , generated by direct EIE and not mediated by the CNT (Fig. 2C; see below). Indeed, the estimated E_a value of 20.8 ± 6.1 kJ mol⁻¹ and PEF = 3.7×10^{-7} (e⁻)⁻¹ nm² fall between the values of pure S_1 and pure T_1 .

We estimated the reaction rate of the recently reported dimerization of C_{60} sandwiched between two graphene sheets at 60 kV (Fig. 4E caption) (37), and obtained $\ln(k) = -21.9$. This data placed at 298 K in Fig. 4E (dark green, x) lies close to our 60-kV data.

Triplet Dimerization of a $(C_{60})_2@oxCNT$. The oxCNT (Fig. 2B), prepared using $KMnO_4$ oxidation of a CNT (44), has both the π - and σ -carbon skeletons destroyed by chemical oxidation, as demonstrated by infrared (IR) absorption (due to benzophenone-like groups) (45). It is reported to be a triplet sensitizer in solution, as efficient as benzophenone, and has a triplet energy lower than ~2.5 eV (46). We encapsulated C_{60} in oxCNT and studied 30–52 vdW C_{60} dimers ($(C_{60})_2@oxCNT$).

The time course of the dimerization events at 120 kV, with a constant EDR of 3.1×10^5 e⁻ nm⁻² s⁻¹, is shown in Fig. 5A, and the frequency integrated over time in Fig. 5B. The semilogarithmic plot in Fig. 5C gives the reaction rates at temperatures between 378 and 453 K, and the Arrhenius plot gives the E_a and PEF values (Fig. 5D). The data agree with values obtained for a prCNT at 80 kV (Fig. 4E), suggesting a triplet mechanism (Fig. 5E).

C_{60} dimerization at 103–203 K occurred with induction period (Fig. 6C) (19), during which the π -conjugation of the CNTs was destroyed, as seen in Fig. 6A and B (47). After the induction period, a steady first-order reaction took place. We measured the reaction rate and obtained $E_a = 1.7 \pm 0.6$ kJ mol⁻¹ and PEF = 1.3×10^{-7} (e⁻)⁻¹ nm² (Fig. 6D).

The remarkably low E_a value suggests an RC, which is formed by ionization and is expected to be extremely reactive (Fig. 6E). RC formation is expected by the standard damage mechanism of radiolysis (3).

Table 1 summarizes the E_a and PEF data in pr-, ox-, and dmCNTs of the four reaction types (Fig. 1B–E). The kinetic profiles are color coded in black, blue, green, and purple. We consider that the path with E_a values of 32.9 – $33.5 \pm \sim 6$ kJ mol⁻¹ in Table 1A (black) took place via S_1 , first because a high-energy e-beam excites CNT with conservation of spin angular momentum, and second because the values compare favorably (within experimental error) with an E_a value of 28 kJ mol⁻¹ (a value calculated from Fig. 5 of ref 48) reported theoretically for S_1 [2 + 2] cycloaddition in gas phase (48). We assign the E_a values of 11–15 kJ mol⁻¹ in Table 1B as obtained for the oxCNT to the T_1 pathway (41) because an oxCNT is an effective triplet sensitizer due to aromatic ketone residues that accelerate relaxation of singlet to triplet (49). The low values of E_a agree with the biradical character of the T_1 excited state of C_{60} . Similarly, we assign T_1 to the 80-keV experiment in a prCNT (Table 1A) because the kinetic data agree with those for an oxCNT in Table 1B. The value of 20.8 kJ mol⁻¹ at 60 keV in Table 1A (green) coincides with a value of 23 kJ mol⁻¹ determined for photodimerization possibly reflecting ISC from singlet to triplet possibly in a 1:3 ratio (50).

Discussion

The SMART-EM study on the electron-impact promoted [2 + 2] cycloaddition mediated by CNTs (Fig. 7) is unique in that we can study in situ the individual reaction events one by one as they take place. The first stage is a fast EIE reaction, characterized by the PEF data. The second stage is a slow thermally driven reaction of excited C₆₀ going across an energy barrier with a frequency of $\exp(-E_a/RT)$. We determined the kinetic parameters separately for the two steps by visually monitoring the individual events of the forward cycloaddition of vdW complexes, which excludes the contribution of cycloreversion and reversible collisions from the kinetic data analysis.

The $\ln(\text{PEF})$ values represent $\ln(k)$ at $T = \text{infinite}$, and they vary widely between -7.9 and -16.4 ($\text{PEF} = 3.9 \times 10^{-4} - 1.3 \times 10^{-7} (\text{e}^-)^{-1} \text{nm}^2$). They are also extremely low in absolute magnitude, indicating that a large number of electrons ($1.0 \times 10^3 - 3.0 \times 10^6$ electrons) are required to form one excited or ionized C₆₀ molecule (area of 0.396nm^2) that produces the dimer. The E_a values (slope) reflect the reactivity of these species in the thermal dimerization reaction (Fig. 7, second step).

To describe the efficiency of the reaction, we borrow the concept of external quantum efficiency (EQE) used to evaluate the efficiency of photovoltaic devices—the ratio of the number of electrons and holes generated by a device to the number of incident photons shining on the device from outside. Similarly, we can define the EQE based on the number of dimers formed relative to the TED shining on the CNT. The EQE values of the S₁ reaction in a prCNT and the T₁ reaction in an oxCNT at 120 kV are 9.8×10^{-4} and 2.1×10^{-6} , respectively, indicating that the latter is nearly 1000 times less efficient because of the infrequent formation of the triplet exciton of the CNT. The very low value of the energy attenuation factor ($\sim 10^{-5}$; from $\sim 100 \text{keV}$ to $\sim 2 \text{eV}$) reflects the lack of a mechanism for efficient energy transfer from the e-beam to the CNT and the loss of energy to phonon vibration of the CNT and physicochemical processes.

The Arrhenius plots for the four representative reactions in Fig. 8 summarize the present finding. In accordance with the accepted mechanism of radiation damage, the ionization pathway operates in dmCNT (purple). In prCNT encapsulating C₆₀ (at $>300 \text{K}$), the ionization is suppressed, and much faster excited-state pathways dominate when the energy of the e-beam is $>80 \text{keV}$ (black and blue). When the e-beam energy is 60keV , it does not excite the CNT and hence C₆₀.

The S₁ species forms in the reaction of C₆₀@prCNT at 120 kV (black) that took place most frequently (the largest $\ln(\text{PEF})$ value of -7.9). The other three pathways via EIE or EII occurred ~ 500 times less frequently. Extremely reactive RC (purple) reacted with near-zero E_a and very small $\ln(\text{PEF}) = -15.9$ (51). We estimate the $\ln(\text{PEF})$ of CAD of C₆₀ to be ~ -25 to -27 , shown as a gray band in Fig. 8, based on the $\ln(\text{PEF})$ of RC and the reported frequency difference of $\sim 10^5$ between CAD and radiolysis of polymers (52). Because CAD is temperature independent (37), we estimate $\ln(k)$ to be ~ -25 to -27 . Thus, the carbon loss of C₆₀ would occur approximately 10^{-5} times more slowly than that of the excited-state reactions. We thus expect CAD to become noticeable only after irradiation with TED of 10^9 – 10^{11} , a dose 100 times greater than that used for SMART-EM imaging. The probability of the atom displacement depends on the elastic scattering cross section, which decreases as the atomic number decreases.

Putting together the above experimental data and the literature information, we suggest, in Fig. 9, the two mechanistic possibilities of radiolysis/ionization of the specimen (Fig. 9A) and excitation (Fig. 9B,C). They are admittedly incomplete but may serve as a cornerstone for future quantitative studies of radiation chemistry under TEM observation conditions using a high-energy e-beam. Fig. 9A-1 shows ionization of the π -rich C₆₀, the standard mechanism of radiation damage (Fig. 1F) (52). We found this path at 103 – 203K in a dmCNT, and consider that it also accounts for the CNT damage at low temperatures (cf. Fig. 6A,B). Fig. 9A-2 illustrates C₆₀ ionization followed by charge neutralization by prCNT and generation of S₀, S₁, or T₁ C₆₀ (Fig.

1E). We observed this path at 60 kV (36). In prCNT and with 100–120-keV electrons (Fig. 9B), the e-beam generates singlet exciton of CNT, and energy transfer forms $S_1 C_{60}$ (Fig. 1B). However, the 80-keV electron can only form a less energetic triplet exciton to generate $T_1 C_{60}$ (Fig. 1C). In Fig. 9C, oxCNT generates a triplet exciton and then forms $T_1 C_{60}$ (Fig. 1E). Note that oxCNT has been known to form triplet excitons, probably because of rapid singlet-to-triplet relaxation.

In summary, the kinetics data summarized in Fig. 8 have shown the importance of VT/VV kinetic analysis in the studies of radiation damage, and show that chemical ionization and electron excitation are inseparable but different mechanisms of the radiation damage, which have often been classified loosely under the single term “ionization.” The data also showed that the conducting prCNT with its high-lying filled orbital not only protects the molecule from radiolysis (8) (Fig. 2C) but can cause selective chemical reactions if suitable orbital interactions between the molecule and the CNT are available. The complexity of the kinetics of EII and EIE suggests a risk in making any mechanistic interpretations of chemical events seen using TEM without performing VT/VV kinetic analysis. The results also illustrated the potential of “cinematic chemistry,” microscopic imaging of dynamic chemical events, for elucidation of the mechanisms of chemical reactions (40).

Materials and Methods

Materials. Single-walled carbon nanotubes (CNTs, Meijo Arc SO, produced by arc-discharge using Ni and Y catalysts, >99% purity, average diameter 1.4 nm, Lot # 6601316) were purchased from Meijo Nano Carbon Co. Ltd. C_{60} powder (nanom purple ST, >98% purity) was purchased from Frontier Carbon Corporation. TEM grids precoated with a lacey microgrid (RO-C15, for VT experiments; pore size 3–8 μm and carbon thickness 70 nm) were purchased from Okenshoji Co., Ltd. Toluene was purchased from Wako Pure Chemical Industries and purified using a solvent purification system (GlassContour) (53) equipped with columns of activated alumina and supported copper catalyst (Q-5) prior to use. Potassium permanganate was purchased from Tokyo Chemical Industry Co., Ltd and sulfuric acid was purchased from Wako Pure Chemical Industries.

General. The water content of the solvent was determined using a Karl Fischer moisture titrator (CA-21, Mitsubishi) to be <10 ppm. Bath sonication for the dispersion of CNTs in toluene was carried out with a Honda Electronics WT-200-M instrument. Oxidative removal of the terminal caps of CNTs was carried out in an electric furnace ASH ARF-30KC. Encapsulation of C_{60} into CNTs was carried out in an electric furnace ASH AMF-20, equipped with a temperature controller AMF-9P. IR spectra were recorded on a JASCO FT/IR-6100 instrument with attenuated total reflection. X-ray photoelectron spectroscopy analysis was carried out on a JPS-9010MC instrument using Mg $K\alpha$ X-rays (1253.6 eV).

Preparation of samples for SMART-EM. The $C_{60}@CNTs$ prepared above are in solid form and thus difficult to deposit directly on a TEM microgrid. We therefore first dispersed samples in toluene (0.01 mg/mL), in vials, which were then placed in a bath sonicator for 1 h. The aim was to soften the samples so that we could secure intimate contact between the CNTs and the carbon surface of the grid. A 10 μL solution of the dispersion was then deposited on a TEM grid placed on a paper that absorbs excess toluene. The resulting TEM grid was dried in vacuo (60 Pa) for 2 h.

SMART-EM observation. Atomic-resolution TEM observations were carried out on a JEOL JEM-ARM200F instrument equipped with an aberration corrector and cold-field emission gun (point resolution 0.10 nm) at acceleration voltages of $E = 60, 80, 100,$ and 120 kV, under 1×10^{-5} Pa in the specimen column, and with typical spherical aberration values of 1–3 mm. Calibration of the

EDR was conducted following a method described in a previous report (19) C_{60} dimerization at 60–120 kV and C_{60} dimerization in oxCNT were monitored at the temperatures mentioned in the main text and an EDR (the number of electrons per second per nm^2) of ca. $3.1 \times 10^5 \text{ e}^- \text{ nm}^{-2} \text{ s}^{-1}$ for 120 kV and $5.0 \times 10^6 \text{ e}^- \text{ nm}^{-2} \text{ s}^{-1}$ for 60–100 kV at 800,000 \times magnification. The imaging instrument was a CMOS camera (Gatan OneView, 4,096 \times 4,096 pixels), operated in binning 2 mode (output image size 2,048 \times 2,048 pixels, pixel resolution 0.20 nm at 1,000,000 \times). A series of TEM images was recorded every 0.5 s as a superposition of 25 consecutive images of 0.04-s frames (automatically processed on Gatan DigitalMicrograph software) over 5–15 min.

We first surveyed C_{60} encapsulated in CNTs on the screen at 200,000 \times magnification to identify CNTs for reaction monitoring. Having found bundles of CNTs suitable for kinetic studies, we stopped the beam irradiation and changed the magnification to 800,000 \times . After waiting for 1 min, until thermal drift of the grid ceased or it was at least relatively relaxed, we commenced observation and movie recording. Focusing was carried out during the collection of images, which was recorded at slightly under-focus conditions (defocus value 10–20 nm). At 80, 100, and 120 kV, we continuously focused on 25–70 molecules in total, with a frame rate of 1.0 s for 5–15 min, until most of the C_{60} molecules oligomerized to form an inner nanotube. At 60 kV, the recording time was set to be 15–20 min, following the results of kinetic studies at 80 kV.

Temperature control. The temperatures were controlled by using a heating holder (JEOL EM-21130). The accuracy of the grid temperature was 2–3 degrees (according to the instrument specifications). After the stage temperature was raised to the setting value, we waited at least 30 min before commencing observations, in order to stabilize the stage for minimization of thermal drift.

Image processing. The images were collected as a .dm3 or .dm4 format file on Gatan DigitalMicrograph software and processed using ImageJ 1.47t software for .dm3 files (54).

Visual data analysis for counting reaction events of C_{60} dimerization. The products of C_{60} dimerization were visually identified following a protocol described in a previous report (19), where molecular structures of [2 + 2] cycloadducts were studied thoroughly using atomic-resolution TEM imaging combined with TEM simulations. The progress of the reactions was studied by analyzing the movies backward, from the end of the reaction, to identify C_{60} dimerization. This procedure eliminates complications due to the intervention of equilibrium caused by thermal cycloreversion. The kinetics of cycloaddition between the fused dimer of C_{60} molecules and C_{60} was excluded from the analysis because the resultant product could possess very different properties.

Acknowledgments

We thank Profs Yuriko Ono, Tetsuya Taketsugu, and Riichiro Saito for fruitful discussions on theoretical aspects of the study. This research is supported by Japan Society for the Promotion of Science (JSPS) KAKENHI (JP19H05459, JP20K15123, and JP21H01758). D. Liu thanks JSPS and the Program of Excellence in Photon Science for a predoctoral fellowship. S.K. thanks MEXT (ALPS program). D. Lungerich thanks JSPS, the Alexander von Humboldt Foundation, and the Institute for Basic Science (IBS-R026-Y1) for financial support.

References

1. M. Knoll, E. Ruska, Das Elektronenmikroskop. *Z. Phys.* **78**, 318–339 (1932).

2. D. B. Williams, C. B. Carter, "Inelastic Scattering and Beam Damage" in *Transmission Electron Microscopy: A Textbook for Materials Science*, (Springer US, 2009), pp. 53–71.
3. R. F. Egerton, Radiation damage to organic and inorganic specimens in the TEM. *Micron* **119**, 72–87 (2019).
4. Z. Cai, S. Chen, L.-W. Wang, Dissociation path competition of radiolysis ionization-induced molecule damage under electron beam illumination. *Chem. Sci.* **10**, 10706–10715 (2019).
5. Z. Liu, K. Yanagi, K. Suenaga, H. Kataura, S. Iijima, Imaging the dynamic behaviour of individual retinal chromophores confined inside carbon nanotubes. *Nat. Nanotechnol.* **2**, 422–425 (2007).
6. T. Okazaki, et al., Coaxially Stacked Coronene Columns inside Single-Walled Carbon Nanotubes. *Angew. Chem., Int. Ed.* **50**, 4853–4857 (2011).
7. T. W. Chamberlain, et al., Isotope Substitution Extends the Lifetime of Organic Molecules in Transmission Electron Microscopy. *Small* **11**, 622–629 (2015).
8. K. Harano, et al., Conformational Analysis of Single Perfluoroalkyl Chains by Single-Molecule Real-Time Transmission Electron Microscopic Imaging. *J. Am. Chem. Soc.* **136**, 466–473 (2014).
9. Y. Iizumi, et al., Molecular Arrangements of Corannulene and Sumanene in Single-Walled Carbon Nanotubes. *ChemNanoMat* **4**, 557–561 (2018).
10. E. Nakamura, Atomic-Resolution Transmission Electron Microscopic Movies for Study of Organic Molecules, Assemblies, and Reactions: The First 10 Years of Development. *Acc. Chem. Res.* **50**, 1281–1292 (2017).
11. K. Harano, K. Minami, E. Noiri, K. Okamoto, E. Nakamura, Protein-coated nanocapsules via multilevel surface modification. Controlled preparation and microscopic analysis at nanometer resolution. *Chem. Commun.* **49**, 3525–3527 (2013).
12. J. Palotás, et al., Incidence of Quantum Confinement on Dark Triplet Excitons in Carbon Nanotubes. *ACS Nano* **14**, 11254–11261 (2020).
13. Pichler, T.; Knupfer, M.; Golden, M. S.; Fink, J.; Rinzler, A.; Smalley, R. E. Localized and Delocalized Electronic States in Single-Wall Carbon Nanotubes. *Phys. Rev. Lett.* **80**, 4729–4732 (1998).
14. Y. Sato, M. Terauchi, High-Energy Resolution Electron Energy-Loss Spectroscopy Study of Interband Transitions Characteristic to Single-Walled Carbon Nanotubes. *Microsc. Microanal.* **20**, 807–814 (2014).
15. P. Börner, U. Kaiser, O. Lehtinen, Evidence against a universal electron-beam-induced virtual temperature in graphene. *Phys. Rev. B* **93**, 134104 (2016).
16. T. Susi, J. C. Meyer, J. Kotakoski, Quantifying transmission electron microscopy irradiation effects using two-dimensional materials. *Nat. Rev. Phys.* **1**, 397–405 (2019).
17. B. W. Smith, M. Monthieux, D. E. Luzzi, Encapsulated C₆₀ in carbon nanotubes. *Nature* **396**, 323–324 (1998).

18. M. Koshino, et al., Analysis of the reactivity and selectivity of fullerene dimerization reactions at the atomic level. *Nat. Chem.* **2**, 117–124 (2010).
19. S. Okada, et al., Direct Microscopic Analysis of Individual C₆₀ Dimerization Events: Kinetics and Mechanisms. *J. Am. Chem. Soc.* **139**, 18281–18287 (2017).
20. M. Koshino, et al., Imaging of Single Organic Molecules in Motion. *Science* **316**, 853, (2007).
21. E. Nakamura, et al., Imaging of Conformational Changes of Biotinylated Triamide Molecules Covalently Bonded to a Carbon Nanotube Surface. *J. Am. Chem. Soc.* **130**, 7808–7809 (2008).
22. H. Hanayama, J. Yamada, I. Tomotsuka, K. Harano, E. Nakamura, Rim Binding of Cyclodextrins in Size-Sensitive Guest Recognition. *J. Am. Chem. Soc.* **143**, 5786–5792 (2021).
23. J. Xing, L. Schweighauser, S. Okada, K. Harano, E. Nakamura, Atomistic structures and dynamics of prenucleation clusters in MOF-2 and MOF-5 syntheses. *Nat. Commun.* **10**, 3608 (2019).
24. T. Nakamuro, M. Sakakibara, H. Nada, K. Harano, E. Nakamura, Capturing the Moment of Emergence of Crystal Nucleus from Disorder. *J. Am. Chem. Soc.* **143**, 1763–1767 (2021).
25. R. Egerton, Radiation Damage and Nanofabrication in TEM and STEM. *Microsc. Today* **29**, 56–59 (2021).
26. N. J. Turro, V. Ramamurthy, J. C. Scaiano, “Transitions between States: Photophysical Processes” in Principles of Molecular Photochemistry: An Introduction, (University Science Books, 2009), pp. 109–168.
27. N. Ohmori, T. Suzuki, M. Ito, Why does intersystem crossing occur in isolated molecules of benzaldehyde, acetophenone, and benzophenone? *J. Phys. Chem.* **92**, 1086–1093 (1988).
28. V. May, O. Kühn, “Excitation Energy Transfer” in Charge and Energy Transfer Dynamics in Molecular Systems, (John Wiley & Sons, Ltd, 2011), pp. 467–558.
29. M. Inokuti, Inelastic Collisions of Fast Charged Particles with Atoms and Molecules---The Bethe Theory Revisited. *Rev. Mod. Phys.* **43**, 297–347 (1971).
30. M. Allan, Study of triplet states and short-lived negative ions by means of electron impact spectroscopy. *J. Electron Spectrosc. Relat. Phenom.* **48**, 219–351 (1989).
31. L. J. Carlson, T. D. Krauss, Photophysics of Individual Single-Walled Carbon Nanotubes. *Acc. Chem. Res.* **41**, 235–243 (2008).
32. S. Bandow, M. Takizawa, K. Hirahara, M. Yudasaka, S. Iijima, Raman scattering study of double-wall carbon nanotubes derived from the chains of fullerenes in single-wall carbon nanotubes. *Chem. Phys. Lett.* **337**, 48–54 (2001).
33. A. M. Rao, et al., Photoinduced Polymerization of Solid C₆₀ Films. *Science* **259**, 955–957 (1993).
34. Y. Wang, J. M. Holden, Z.-H. Dong, X.-X. Bi, P. C. Eklund, Photo-dimerization kinetics in solid C₆₀ films. *Chem. Phys. Lett.* **211**, 341–345 (1993).
35. S. Han, et al., Microscopic mechanism of fullerene fusion. *Phys. Rev. B* **70**, 113402 (2004).

36. U. Kaiser, *et al.*, Transmission electron microscopy at 20 kV for imaging and spectroscopy. *Ultramicroscopy* **111**, 1239–1246 (2011).
37. R. Mirzayev, *et al.*, Buckyball sandwiches. *Sci. Adv.* **3**, e1700176 (2017).
38. J. W. Jordan, *et al.*, Single-molecule imaging and kinetic analysis of intermolecular polyoxometalate reactions. *Chem. Sci.* **12**, 7377–7387 (2021).
39. K. J. Laidler, “Elementary Gas-Phase Reactions” In *Chemical Kinetics*, (Pearson, 1987), pp. 137–182.
40. T. Shimizu, *et al.*, Real-Time Video Imaging of Mechanical Motions of a Single Molecular Shuttle with Sub-Millisecond Sub-Angstrom Precision. *Bull. Chem. Soc. Jpn.* **93**, 1079–1085 (2020).
41. M. R. Fraelich, R. B. Weisman, Triplet states of fullerene C₆₀ and C₇₀ in solution: long intrinsic lifetimes and energy pooling. *J. Phys. Chem.* **97**, 11145–11147 (1993).
42. D. L. Bunker, W. L. Hase, On non - RRKM unimolecular kinetics: Molecules in general, and CH₃NC in particular. *J. Chem. Phys.* **59**, 4621–4632 (1973).
43. Y. Yomogida, *et al.*, Industrial-scale separation of high-purity single-chirality single-wall carbon nanotubes for biological imaging. *Nat. Commun.* **7**, 12056 (2016).
44. K. A. Wepasnick, Surface and structural characterization of multi-walled carbon nanotubes following different oxidative treatments. *Carbon* **49**, 24–36 (2011).
45. U. J. Kim, C. A. Furtado, X. Liu, G. Chen, P. C. Eklund, Raman and IR Spectroscopy of Chemically Processed Single-Walled Carbon Nanotubes. *J. Am. Chem. Soc.* **127**, 15437–15445 (2005).
46. C.-Y. Chen, R. G. Zepp, Probing Photosensitization by Functionalized Carbon Nanotubes. *Environ. Sci. Technol.* **49**, 13835–13843 (2015).
47. K. Urita, K. Suenaga, T. Sugai, H. Shinohara, S. Iijima, In Situ Observation of Thermal Relaxation of Interstitial-Vacancy Pair Defects in a Graphite Gap. *Phys. Rev. Lett.* **94**, 155502 (2005).
48. V. Zobač, *et al.*, Photo-induced reactions from efficient molecular dynamics with electronic transitions using the FIREBALL local-orbital density functional theory formalism. *J. Phys.: Condens. Matter* **27**, 175002 (2015).
49. H. Yu, Y. Jin, F. Peng, H. Wang, J. Yang, Kinetically Controlled Side-Wall Functionalization of Carbon Nanotubes by Nitric Acid Oxidation. *J. Phys. Chem. C* **112**, 6758–6763 (2008).
50. M. Sakai, M. Ichida, A. Nakamura, Raman scattering study of photopolymerization kinetics in C₆₀ crystals. *Chem. Phys. Lett.* **335**, 559–566 (2001).
51. M. Hashiguchi, H. Inada, Y. Matsuo, Solution-phase synthesis of dumbbell-shaped C₁₂₀ by FeCl₃-mediated dimerization of C₆₀. *Carbon* **61**, 418–422 (2013).
52. R. F. Egerton, M. Takeuchi, Radiation damage to fullerite (C₆₀) in the transmission electron microscope. *Appl. Phys. Lett.* **75**, 1884–1886 (1999).
53. A. B. Pangborn, M. A. Giardello, R. H. Grubbs, R. K. Rosen, F. J. Timmers, Safe and Convenient Procedure for Solvent Purification. *Organometallics* **15**, 1518–1520 (1996).

54. C. A. Schneider, W. S. Rasband, K. W. Eliceiri, NIH Image to ImageJ: 25 years of image analysis. *Nat. Methods* **9**, 671–675 (2012).

Figures and Tables

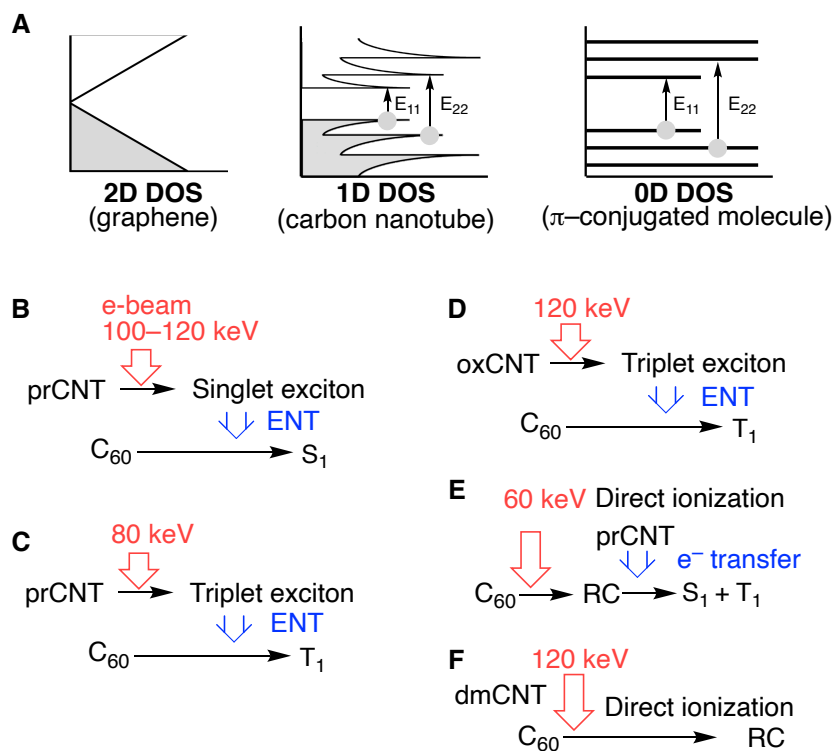


Fig. 1. Density of states (DOS) and pathways of C₆₀ excitation. (A) DOS of 0-D to 2-D materials. (B–F) CNT excitation by EIE and ENT from CNT to C₆₀.

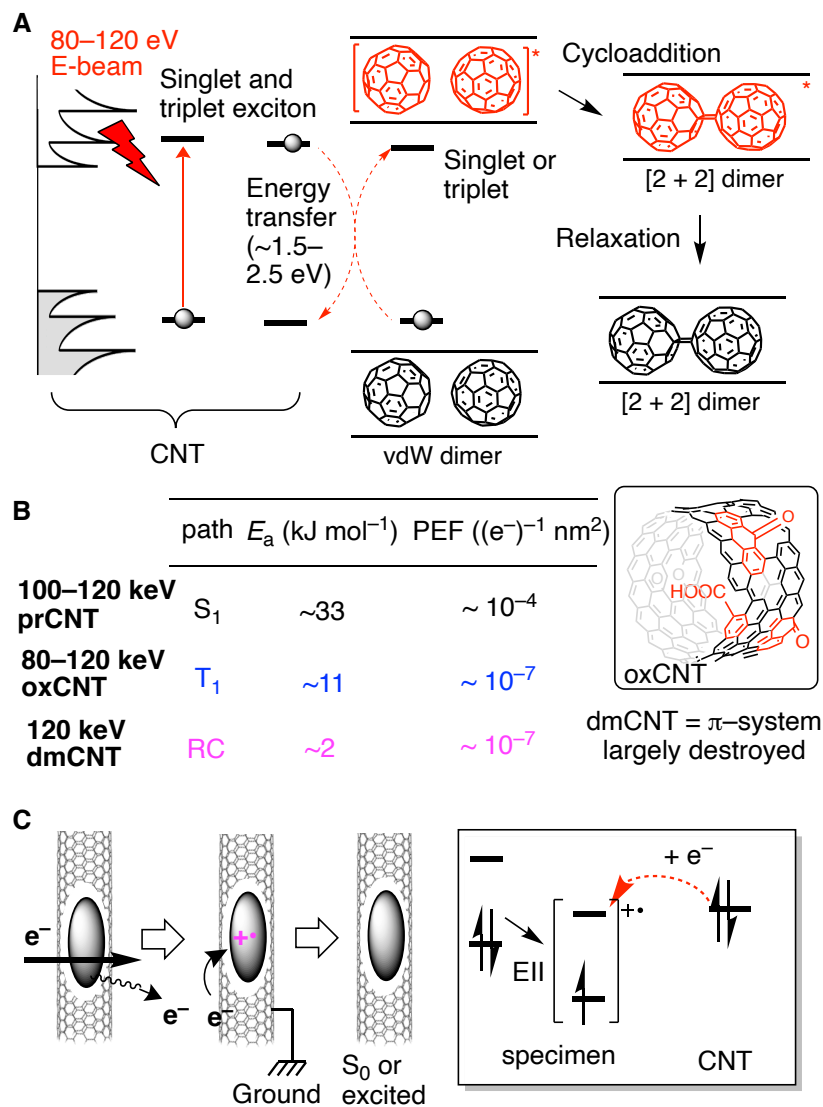


Fig. 2. Electron-impact promoted [2 + 2] cycloaddition mediated by CNT–quasi-1D material. (A) [2 + 2] Dimerization of C₆₀ by EIE of the CNT followed by ENT from the CNT exciton to C₆₀. The E₂₂ transition is shown as a simplified example of transitions responsible for the C₆₀ excitation. (B) Representative kinetic parameters of C₆₀ dimerization under VT/VV conditions. (C) “Grounding” of an ionized specimen molecule by electron transfer from the prCNT.

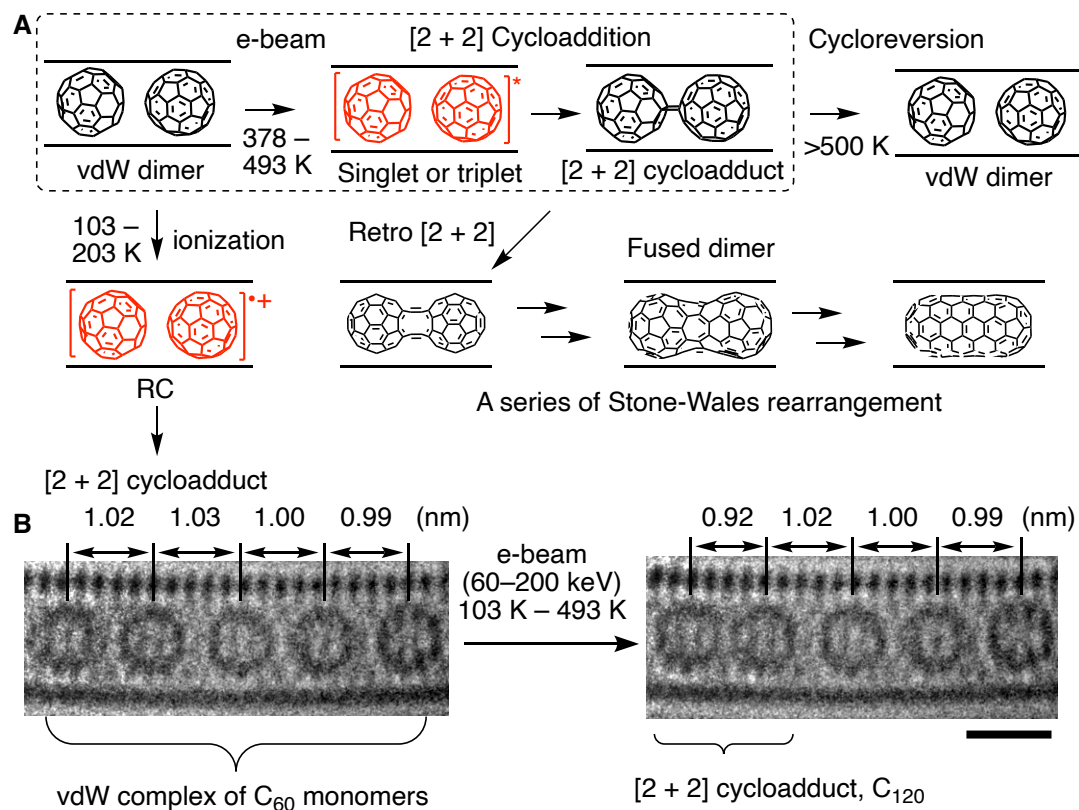


Fig. 3. [2 + 2] Cycloaddition via excited state. (A) Cycloaddition via excited state and RC as well as retro cycloaddition and further fusion to produce a short CNT. (B) TEM images of vdW complexes (intermolecular distance 0.99–1.03 Å) and [2 + 2] dimer (0.92 Å). Fused dimer in (A) shows a characteristic intermolecular distance of 0.8 Å. Scale bar = 1 nm.

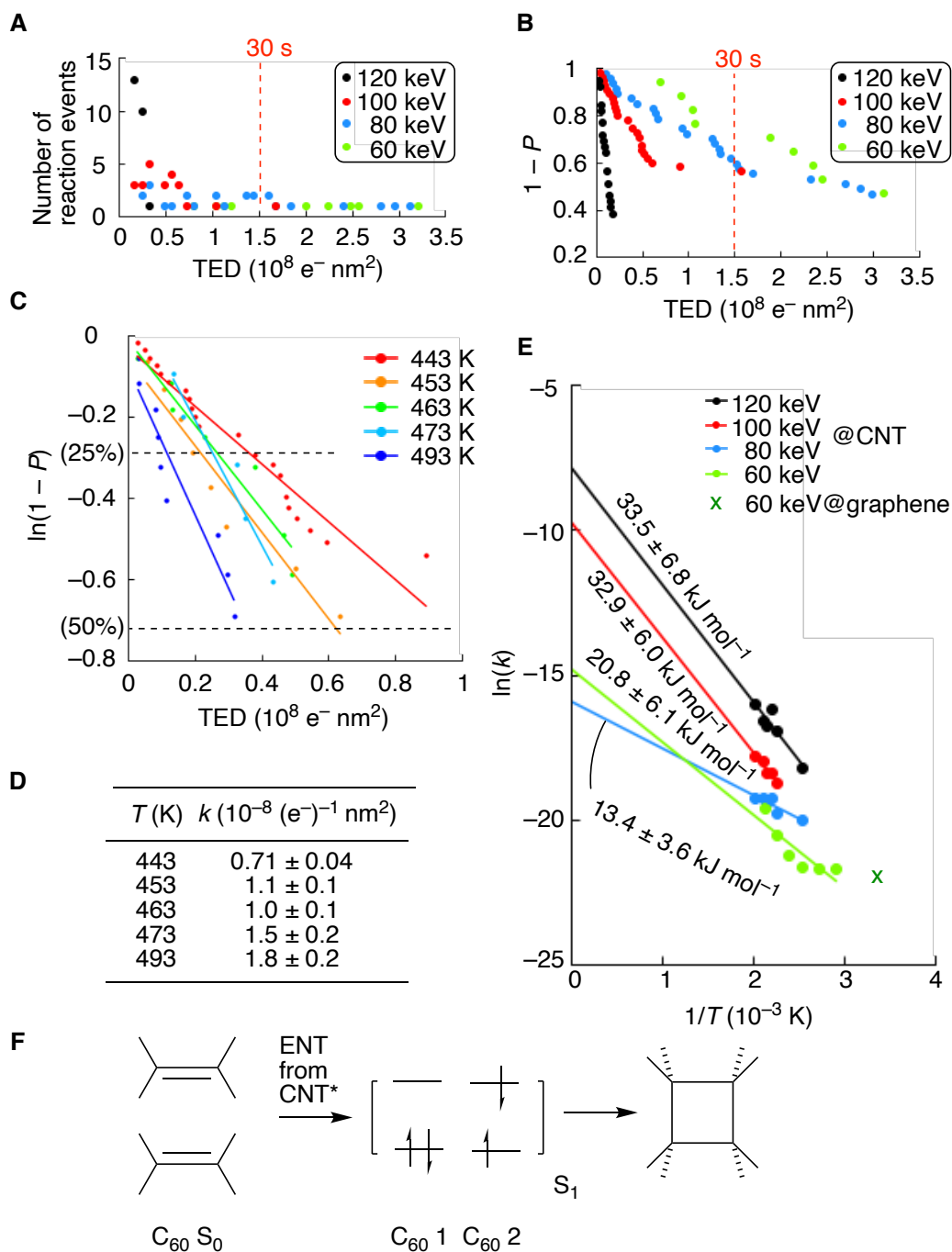


Fig. 4. VT/VV-SMART-EM kinetic study of C_{60} dimerization. (A) Occurrence of stochastic reaction events of C_{60} dimerization integrated over every $8.0 \times 10^6 e^- nm^{-2}$ at 443 K plotted against TED (Table S3, Fig. S2). (B) Reaction progress of C_{60} dimerization at 443 K. (C) Semilogarithmic plot of C_{60} dimerization at 100 kV above 443 K and first-order kinetic fitting shown as solid lines. (D) Reaction rate constants of C_{60} dimerization at 100 kV obtained via linear fitting of (C). (E) Arrhenius plot of C_{60} dimerization. The green plot is for the 60-keV reaction, where the slope at higher temperature ($1/T = 2$ to 2.4×10^{-3}) is close to that of the S_1 path (black, red) and that at lower temperature (2.5 to 3×10^{-3}) is close to the T_1 path (blue). The x indicates the $\ln(k)$ value

for dimerization of C_{60} sandwiched between graphene sheets estimated from Fig. 4 in ref 37. (F)
Mechanistic sketch of the S_1 cycloaddition.

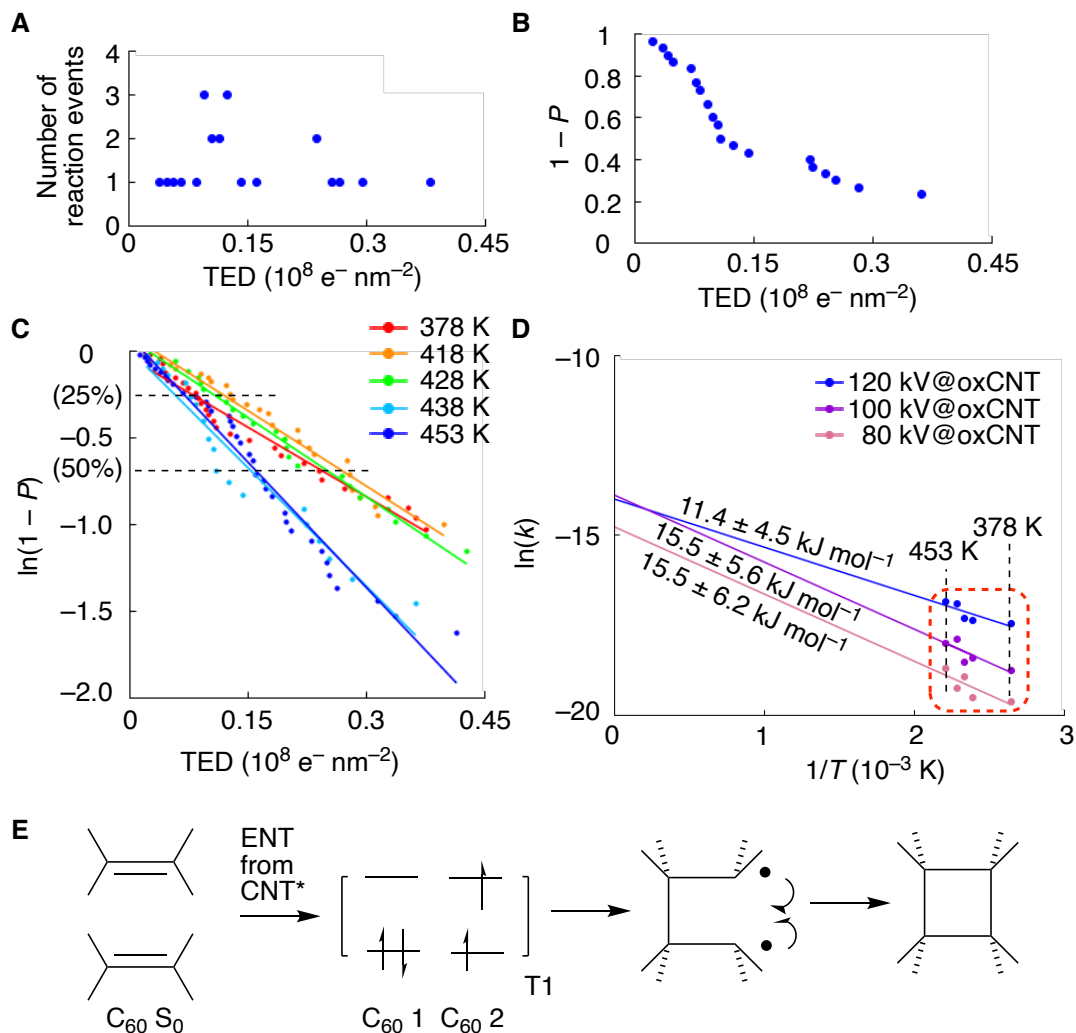


Fig. 5. Kinetic study of C_{60} dimerization in an oxCNT. (A) Occurrence of stochastic reaction events of C_{60} dimerization inside oxCNTs at 120 kV integrated over every $8.0 \times 10^6 e^- nm^{-2}$ at 438 K for a $(C_{60})_2@oxCNT$ plotted against TED (Table S4, Fig. S4-5). (B) Reaction progress of C_{60} dimerization inside oxCNTs at 120 kV. (C) First-order kinetics of C_{60} dimerization inside oxCNTs at 120 kV. (D) Arrhenius plot of C_{60} dimerization inside oxCNTs at 80–120 kV. (E) Mechanistic sketch of the T_1 reaction.

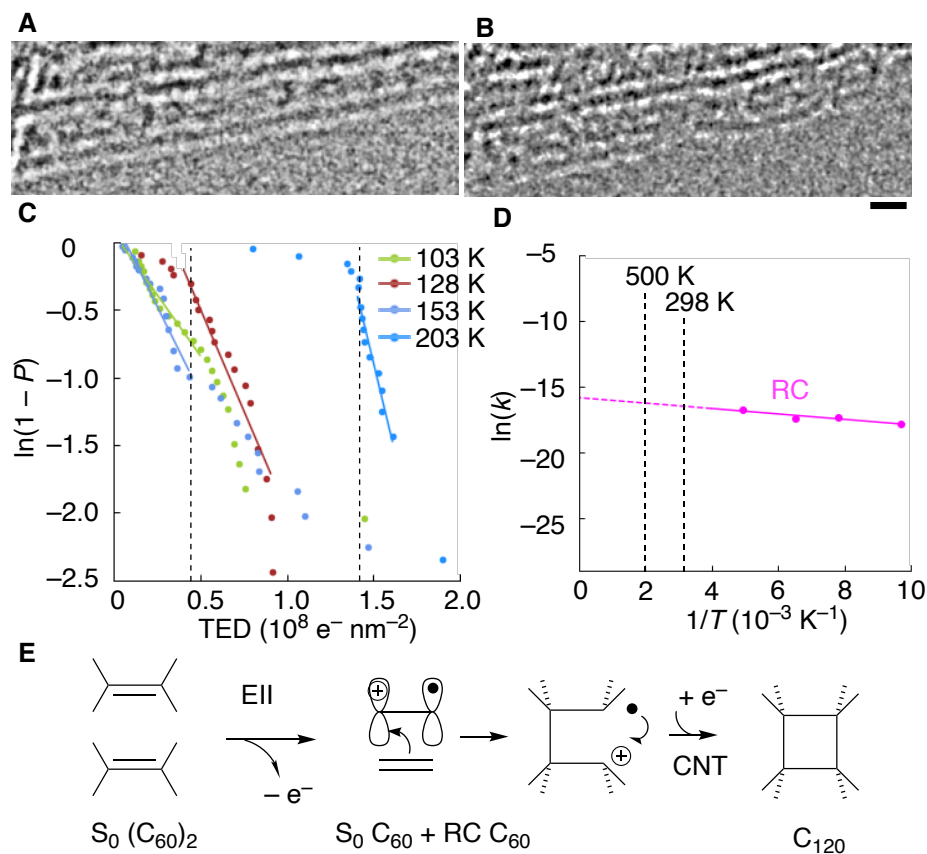


Fig. 6. Dimerization at 103–203 K via RC. (A,B) The $C_{60}@prCNT$ decomposes after prolonged irradiation at 153 K to produce $C_{60}@dmCNT$. Scale bar = 1 nm. (C) First-order kinetics of C_{60} dimerization in dmCNTs at 120 kV. Dotted lines show the end of induction period at 128 K and 203 K, from where the rate was calculated. (D) Arrhenius plot of C_{60} dimerization in a dmCNT at 120 kV. (E) Mechanistic sketch of the RC reaction.

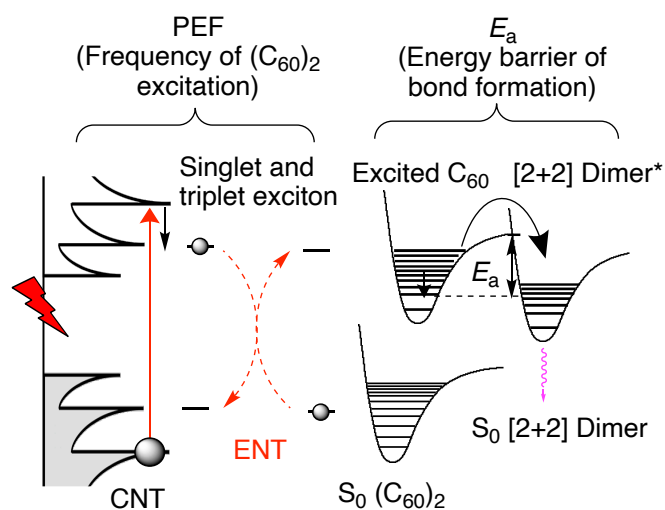


Fig. 7. PEF and E_a , representing EIE/ENT and cycloaddition, respectively. Of two possible mechanisms of ENT, the Förster mechanism of ENT is shown. The E_{22} transition is shown as an example of transitions responsible for C_{60} excitation. The E_{33} transition followed by thermal relaxation is shown as an example of the processes involved in the C_{60} excitation.

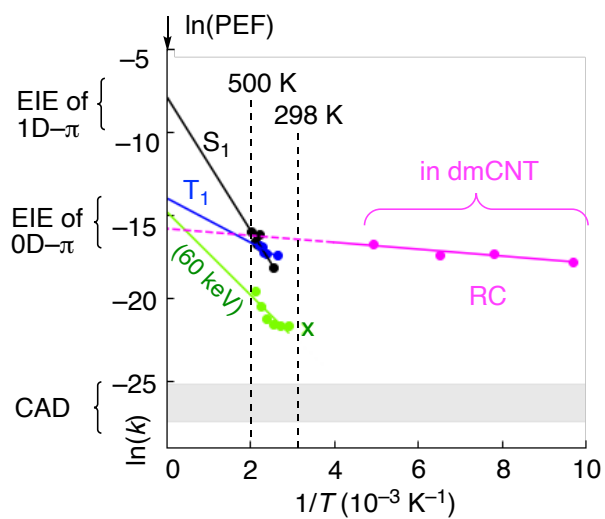
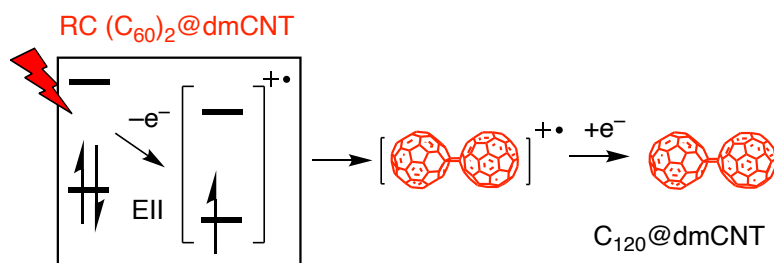


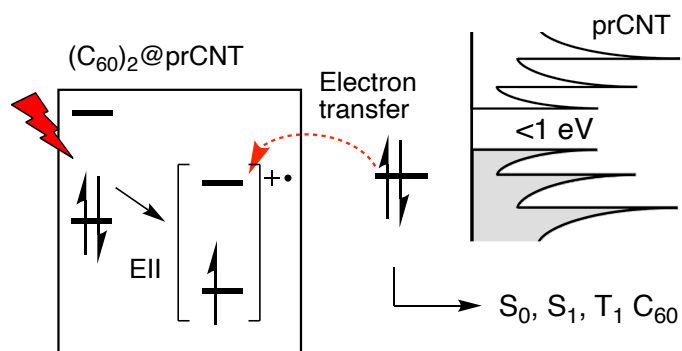
Fig. 8. Arrhenius plot for four representative reactions. Black: The 120-kV data in Table 1A via S_1 . Blue: the 120-kV data in Table 1B via T_1 . Green: the 60-kV data in Table 1A via direct EIE. Purple: the 120-kV data in Table 1C via RC. Gray band: a range of $\ln(k)$ values for temperature-independent CAD estimated from $\ln(\text{PEF})$ of radiolysis. The x indicates the $\ln(k)$ value for dimerization of C_{60} sandwiched between graphene sheets estimated from Fig. 4 in ref 37.

A Direct ionization of C_{60}

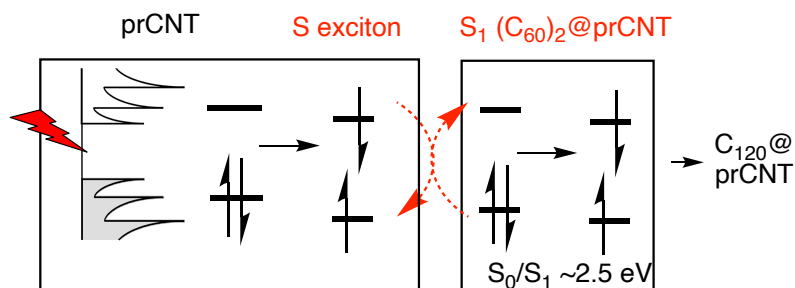
A-1 Direct ionization generates RC of C_{60} (Fig. 1F)



A-2 Ionization/charge neutralization by prCNT (Fig. 1D)



B Singlet exciton of prCNT (Fig. 1B)



C Triplet exciton of oxCNT (Fig. 1D)

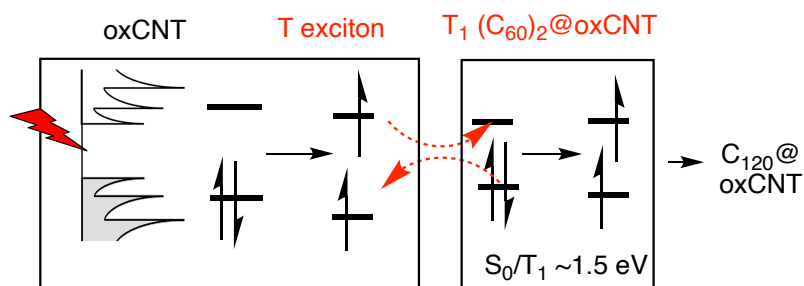


Fig. 9. Four pathways available for activation of vdW $(C_{60})_2@CNT$ for [2 + 2] cycloaddition. (A) Two paths following the initial ionization. (A-1) Ionization of C_{60} to generate radical cation at 103–203 K in a dmCNT. (A-2) Ionization of C_{60} followed by charge neutralization to generate an

excited state taking place with a 60-kV e-beam. (B) Singlet CNT exciton generates $S_1 C_{60}$ with a 100–120-kV e-beam. (C) Triplet oxCNT generates $T_1 C_{60}$ with an 80-kV e-beam.

Table 1. E_a and PEF values obtained from the Arrhenius plot of the C_{60} dimerization events: (A) C_{60} dimerization in a prCNT, (B) in a oxCNT, and (C) in a dmCNT. Color coding according to the reactive species.

A $(C_{60})_2$ @prCNT

e-beam (keV)	E_a (kJ mol ⁻¹)	ln(PEF)	PEF ((e ⁻) ⁻¹ nm ²)	path
120	33.5 ± 6.8	-7.9 ± 1.8	3.9 × 10 ⁻⁴	S ₁
100	32.9 ± 6.0	-9.7 ± 1.6	5.9 × 10 ⁻⁵	S ₁
80	13.4 ± 3.6	-15.9 ± 1.0	1.2 × 10 ⁻⁷	T ₁
60	20.8 ± 6.1	-14.8 ± 1.8	3.7 × 10 ⁻⁷	S ₁ /T ₁

B $(C_{60})_2$ @oxCNT

e-beam (keV)	E_a (kJ mol ⁻¹)	ln(PEF)	PEF ((e ⁻) ⁻¹ nm ²)	path
120	11.4 ± 4.5	-14.0 ± 1.3	8.3 × 10 ⁻⁷	T ₁
100	15.5 ± 5.6	-13.9 ± 1.9	9.3 × 10 ⁻⁷	T ₁
80	15.5 ± 6.2	-14.8 ± 1.8	3.9 × 10 ⁻⁷	T ₁

C $(C_{60})_2$ @dmCNT

e-beam (keV)	E_a (kJ mol ⁻¹)	ln(PEF)	PEF ((e ⁻) ⁻¹ nm ²)	path
120	1.7 ± 0.6	-15.9 ± 0.5	1.3 × 10 ⁻⁷	RC